Materials Transactions, Vol. 59, No. 2 (2018) pp. 230 to 236

Interface-Related Shear Banding Deformation of Amorphous/Crystalline CuZr/Cu Nanolaminates by Molecular Dynamics Simulations

Yan Cui[1], Yoji Shibutani[2,*], Ping Huang[1,*], Fei Wang[3,*], Kewei Xu[1] and Tianjian Lu[3,4]

[1]*State-key Laboratory for Mechanical Behavior of Material, Xi'an Jiaotong University, Xi'an 710049, China*
[2]*Department of Mechanical Engineering, Osaka University, Osaka, Japan*
[3]*State Key Laboratory for Strength and Vibration of Mechanical Structures, School of Aerospace, Xi'an Jiaotong University, Xi'an 710049, China*
[4]*MOE Key Laboratory for Multifunctional Materials and Structures, Xi'an Jiaotong University, Xi'an 710049, China*

Whereas adding a soft crystalline layer into metallic glasses can modify shear banding deformation and enhance plastic deformability, interface-related plastic behavior played a crucial role in the shear banding deformation of amorphous/crystalline nanolaminates (A/CNLs). In this work, the influence of amorphous/crystalline interface (ACI) and grain boundary (GB) on the shear banding deformation of amorphous $Cu_{55(at\%)}Zr_{45(at\%)}$/crystalline Cu nanolaminates were systemically studied using molecular dynamics (MD) simulations. On one hand, ACIs with both [110] and $[1\bar{1}\bar{1}]$ interfacial crystal orientations were constructed. Results showed that localized interfacial sliding initiate at $[1\bar{1}\bar{1}]$ interfacial orientation at an extremely low stress, due mainly to abrupt compositional mixing at the ACI. On the other hand, GB either vertical or parallel to ACI were specially designed. Large numbers of pre-existing boundary dislocation activations along the vertical GB were shown to facilitate the shear banding formation of A/CNLs. In contrast, interfacial dislocation emission and dislocation slip transmission across the parallel GB postponed the shear banding formation. These results enable controlling shear banding deformation of A/CNLs and ensure their reliable application via nanoscale interfacial design. [doi:10.2320/matertrans.M2017286]

(Received September 21, 2017; Accepted November 6, 2017; Published December 22, 2017)

Keywords: *amorphous/crystalline nanolaminate, grain boundary, twin boundary, shear banding, molecular dynamics simulations*

1. Introduction

Amorphous alloys with extremely high strength and hardness have become one of the most promising engineering materials. However, their unique shear banding deformation led to poor plastic deformability, thus seriously limiting their practical applications. Inserting a soft crystalline phase into the amorphous phase was recently found to be an effective method to resolve this issue. Numerous experimental findings[1–7] and molecular dynamics (MD) studies[8–10] had revealed a combination of high strength and good ductility in nanoscaled amorphous/crystalline nanolaminates (A/CNLs). The enhanced strength was attributed to both of the two constituent metallic layers[11], and the better plastic deformability was induced from the easily strain-accommodated amorphous/crystalline interface (ACI).

The atomic structure and interfacial sliding behavior of ACI played decisive roles in the plastic deformation of A/CNLs. The plastic deformation of A/CNLs was mainly determined by the deformation mechanisms of individual layers as well as the plastic transformation between them, especially the plastic transfer at ACI between dislocation activations in crystalline layers and shear transformation zones (STZs) in amorphous layers[4,5]. Because of the unique microstructure and mechanical property of ACI, the plastic deformation mode could vary from localized shear banding deformation to homogeneous co-deformation. ACI possesses a moderate interfaical strength relative to the two constituent layers, which could bear the load and transfer shear strain between the two layers[12–14]. It had been demonstrated that crystalline oritentation greatly affects the interfacial behavior of $Cu_{50}Ta_{50}$/Ta A/CNLs, such as oritentation-dependent layering, crystallication, intermixing and composition segreation[15]. However, the important influence of interfacial crystal oritentation on the shear banding deformation of A/CNLs was rarely discussed, even for the extensively studied amorphous CuZr - crystalline Cu interface.

The shear banding deformation of A/CNLs was also closely linked to the microstructures of nanocrystalline layers. For example, shear bands (SBs) in CuZr/Cu A/CNLs were initialized in CuZr layers due to accumulated glide dislocations along CuZr-Cu interfaces, and then propagated into adjacent Cu layers via slips on (111) plane non-parallel to the interface[6,16]. That is, due to crystallographic constraint of the Cu layers, SBs were approximately parallel to (111) plane in the Cu layer. Actually, nanocrystalline grains synthesized by magnetron sputtering typically grow with columnar morphology along the deposition growth direction[17,18], and contain highly distributed defects such as pre-storage dislocations, grain boundaries (GB) and nanoscale twin boundaries (TB)[6,19–21]. GB planar defects consisting of a group of dislocations often play crucial roles in the mechanical behavior of nanocrystalline metals[22]. As a dislocation source in A/CNLs, GB may play an indispensable role in the formation and propagation of SBs. Relative to the general GB, TB was considered as a mechanically stable barrier to dislocation movement, and the twinning-related mechanism could lead to both strengthening and toughening materials via twin-dislocation interactions[23–26]. In addition, shear localization along TBs under cyclic deformation without dislocation pile-up like the conventional GB was reported by Li *et al.*[27] Therefore, dislocation activations in nanocrystal layers associated with highly distributed GB and TB must affect significantly the plastic deformation of A/CNLs. However, existing studies on the plastic deforma-

*Corresponding authors, E-mail: huangping@mail.xjtu.edu.cn; sibutani@mech.eng.osaka-u.ac.jp; wangfei@mail.xjtu.edu.cn

tion of A/CNLs used to consider the microstructure of crystalline layers as the boundary-free condition. To get a more precise control of the nanoscale interfacial design of A/CNLs, shear banding deformation mechanisms related to crystal boundaries must be achieved.

In the current study, the plastic deformation behaviors of CuZr/Cu A/CNLs under pure shear were systematically studied using MD simulations, with special focus placed upon two issues. One is the interfacial oritentation-dependent shear banding deformation of A/CNLs. For this purpose, CuZr/Cu ACIs with different interfacial crystal orientations were constructured, with pure amorphous CuZr taken as reference. Another is the influence of GB and TB within crystalline layers on the shear banding deformation of A/CNLs. To this end, crystalline boundaries vertical and parallel to ACI were separately constructed.

2. Simulation Method

Large-scale Atomic/Molecular Massively Parallel Simulator (LAMMPS)[28] was used to perform MD simulations. Amorphous $Cu_{50}Zr_{50}$ (subscript being the atomic volume fraction of each element) and amorphous $Cu_{50}Zr_{50}$/crystalline Cu/amorphous $Cu_{50}Zr_{50}$ nanolaminated structures were constructed with periodic boundary conditions. Interaction between Cu and Zr atoms was described using an embedded atom method potential for CuZr alloy systems[29]. Pure amorphous $Cu_{50}Zr_{50}$ model (labeled as amorphous CuZr) was built by melting at 2000 K and cooling down subsequently to 50 K at 0.01 K/ps. All the A/CNLs models comprised nanocrystalline Cu layer and amorphous CuZr layer, and the amorphous CuZr phase had the same cooling process as the pure amorphous model. The dimensions of all the simulated unit models were $20 \times 20 \times 6$ nm^3. The crystalline Cu layer and the amorphous CuZr layer were both 10 nm along the x-aixs, as shown in Fig. 1(a). The A/CNLs models were designed with orientations of GB and TB in crystalline layers shown in Fig. 1(b), either vertical or parallel to the ACI. Figs. 1(c) (d) (e) (f) were the xz in-plane structures (yellow plane in Fig. 1(a)) of the four structural configurations of A/CNLs models, labeled as A/CNL+$GB_{vertical}$, A/CNL+$GB_{parallel}$, A/CNL+$TB_{vertical}$ and A/CNL+$TB_{parallel}$, respectively. For comparison, a A/CNL model without any boundaries in crystalline layer (labeled as A/CNL) was also constructed.

GB and TB within the A/CNLs were both constructed using the relative crystallographic rotation of two Cu grains. The crystallographic orientation of grain 1 (G1) was pre-set as [110] along the x-axis, $[\bar{1}1\bar{2}]$ along the y-axis and $[\bar{1}11]$ along the z-axis. For A/CNL+$GB_{vertical}$ and A/CNL+$TB_{vertical}$ models, the other grain was obtained by anticlockwise tilting of G1 along the x-axis. For A/CNL+$GB_{parallel}$ model, the right grain was obtained with anticlockwise tilting of G1 along the z-axis. To explore the influence of interfacial crystal orientation on plastic deformation of A/CNLs, the $[1\bar{1}\bar{1}]$ crystal orientation (namely the dislocation slip plane in FCC Cu) parallel to the ACI plane in A/CNL+$TB_{parallel}$ model was constructed. As a result, the interfacial crystal orientations of [110] and $[1\bar{1}\bar{1}]$ could be compared in A/CNL model and A/CNL+$TB_{parallel}$ model, respectively. To ensure reliable misorientation angles and reasonable boundary energy of each boundary configuration, the GB energy (γ_{GB}) with each misorientation angle was systematically estimated by:

$$\gamma_{GB} = \frac{E_{GB} - e_B \times N_{GB}}{2A} \tag{1}$$

$$e_B = \frac{E_B}{N_B} \tag{2}$$

where E_{GB} and N_{GB} are the total energy and the number of atoms of crystalline layer in A/CNL models, respectively. E_B, N_B and e_B are the total energy, the number of atoms, and the per-atomic energy in the simulation box of perfect crystalline Cu, respectively. A is the cross-sectional area of crystalline layer along z-direction. The lowest boundary energy (about 240 mJ/m^2) appeared when the anticlockwise misorientation angle was 109.4°, which was meant to be the coher-

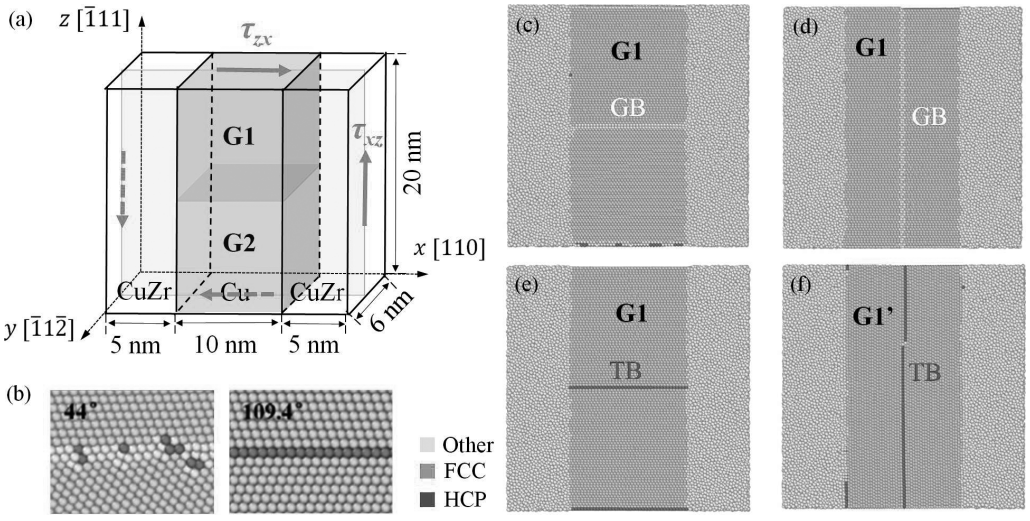

Fig. 1 (a) Schematic diagram of CuZr/Cu A/CNL model and microstructural configurations of four A/CNL models with GB and TB in (b), labeled as (c) A/CNL+$GB_{vertical}$, (d) A/CNL+$GB_{parallel}$, (e) A/CNL+$TB_{vertical}$ and (f) A/CNL+$TB_{parallel}$, in which the directions of vertical and parallel boundaries in crystalline Cu layer were constructed relative to the ACI plane.

ent TB ($\sum 3A$). The boundary with a misorientation angle of 44° was selected to construct a general high-angle GB.

In the present study, all the simulated models were energetically relaxed to obtain the minimum systematic energy before plastic deformation was applied. Periodic boundary conditions were applied on each direction of the model. Nose-Hoover thermostat within the isenthalpic (NPT) ensemble was used to control the motion of atoms. Temperature was controlled as 50 K. Pure shear deformation was conducted at a constant engineering shear strain rate of 10^8 s^{-1}. Plastic deformation of each model was discerned using the software package OVITO[30]. Plastically deformed atoms were colored by atomic von Mises shear strain, η_i^{Mises} [31,32], which was proved to be an effective parameter to characterize locally deformed microstructures.

3. Results and Discussion

3.1 Shear banding behaviors of pure amorphous CuZr

Figure 2(a) displayed the stress versus strain curves of pure amorphous CuZr. The shear stress first increased with the shear strain applied. Upon reaching the maximum shear stress τ_{max} of 1.75 GPa, the plastic flow showed an obvious stress drop and stayed at a plateau afterwards. To better clarify the atomic structure evolution, the *xz* in-plane structures (as illustrated in the yellow plane of Fig. 1(a)) were shown here instead of the 3D structures. It was seen from Figs. 2(b), (c) and (d) that large atomic strain was initially randomly assembled. Upon loading, several atomic clusters having the largest shear strain concentration were assembled along the maximum shear plane, eventually forming a locally narrow SB when the engineering shear strain reached 0.16, the same as in our previous study[13].

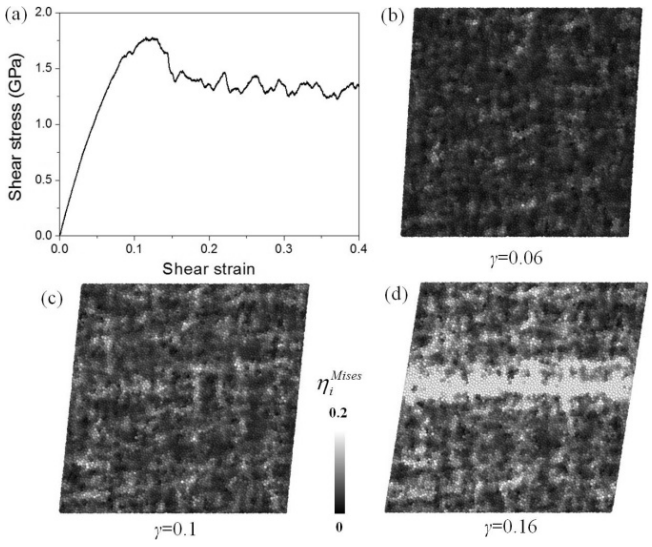

Fig. 2 (a) Shear stress versus shear strain curves of pure amorphous CuZr and (b) (c) (d) microstructure evolution snapshots at engineering shear strain of 0.06, 0.1 and 0.16. Atoms were all colored according to the calculated magnitude of von Mises shear strain η_i^{Mises}.

3.2 Influence of amorphous/crystalline interfaces on shear banding

3.2.1 Shear banding deformation versus homogeneous deformation

Figure 3(a) presented the stress versus strain curves of the A/CNLs model without grain boundary as well as the A/CNL+$TB_{vertical}$ model. Based on the mechanical characteristics of these stress versus strain curves, pure amorphous CuZr was seen to possess the highest shear strength, and the plastic deformation behaviors of A/CNL model and A/CNL+$TB_{vertical}$ structures were similar. No stress drop appeared when the highest shear stress was approached and even strain hardening showed up when the shear strain exceeded about 0.2, which were quite different from the pure amorphous CuZr during deformation.

The numerically predicted plastic deformation behaviors of the A/CNL model with perfect crystal lattice were shown in Figs. 3(b), (c) and (d). In these plots, the periodic boundary was duplicated along the *x*-direction to clarify the whole shear banding deformation of the A/CNL model and the A/CNL+$TB_{vertical}$ model. Atomic strain concentrations were seen to first appear at the ACI. This was mainly because atomic strain concentrations at the ACI were much easier than those within both the amorphous and crystalline layers inner, because of the different atomic structure of two constituent layers and the mismatch of elastic modulus at the ACI. Afterwards, the atomic strain of crystalline layers homogeneously increased while that of the amorphous layers increased heterogeneously, with large atomic strains gradually concentrated within a narrow band in the amorphous layer. When the engineering shear strain reached 0.2, a mature shear banding deformation happened in the amorphous CuZr layer.

The shear banding deformation of the A/CNL+$TB_{vertical}$ model was not shown here because, during the whole plastic deformation, it was very similar to that of the A/CNL without boundary model, which demonstrated that vertical TB in crystalline layers had negligible effect on shear banding deformation of A/CNLs. Nanotwinned metals typically exhibited three types of dislocation-mediated deformation mecha-

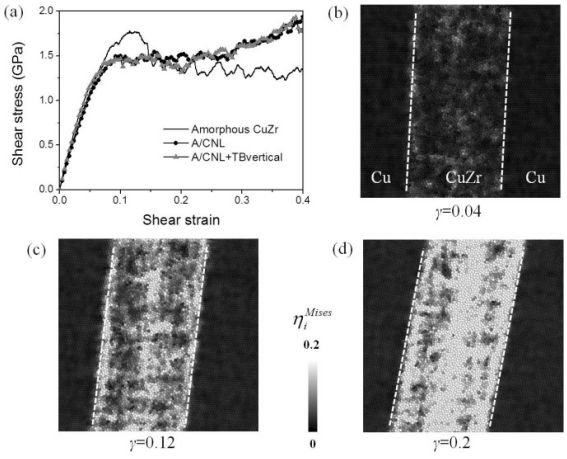

Fig. 3 (a) Stress versus strain curves of A/CNL and A/CNL+$TB_{vertical}$ models compared with pure amorphous CuZr. (b) (c) (d) Microstructure evolution snapshots of A/CNL model in crystalline layer at engineering shear strain of 0.04, 0.12 and 0.2.

nism: dislocation pile-up against and slip transfer across TB, Shockley partials gliding on TB leading to TB migration, and threading dislocations slip confined by neighboring TB. These mechanisms were switchable upon changing the loading direction with respect to TB. Noting that in the present study the shear direction was parallel to the TB plane, the dominant deformation mechanism was supposed to be threading dislocations slip confined by neighboring TB. However, because dislocation nucleation at the coherent TB was impossible and the amorphous layer would yield before the A/C interfacial dislocation emission, the crystalline layer with TB acted in a way similar to the perfect crystalline layer.

3.2.2 Influence of interfacial orientation on the plastic deformation of nanolaminates

The stress versus strain curves shown in Fig. 4(a) revealed that the A/CNL+$TB_{parallel}$ model had a shear strength much lower than that of pure amorphous CuZr. Plastic deformation snapshots displayed in Figs. 4(b) (c) (d) illustrated further that the shear banding deformation mainly happened along the ACI. At the early stage of plastic deformation, locally instable STZs in the amorphous layer at ACI were heterogeneously activated because the interfacial shear strength here was lower than that of the inner layer. With increasing load, atomic strain concentration at ACI gradually became severe and atomic plastic flow took place at both the amorphous side and the crystalline side. As a result, a SB spanning both the amorphous layer and the crystalline layer along ACI was formed even at a very small engineering shear strain (0.05). Subsquently, SB thickening expanding into both amorphous and crystalline layers occurred.

Upon comparing the interfacial crystal orientation of [110] and $[1\bar{1}\bar{1}]$ in A/CNL and A/CNL+$TB_{parallel}$, SB sliding was much easier to occur along $[1\bar{1}\bar{1}]$ interface, leading to the much lower shear strength (about 0.9 GPa) of A/CNL+$TB_{parallel}$. The dependence of crystalline orientation on atomic structure and the plastic behavior of chemically heterogeneous ACIs have attracted considerable research interests and was recently studied by MD simulations[15,33–35]. It was demonstrated that the orientation dependence in interfacial structures led to orientation dependence in interfacial energy, interfacial width, and diffusivity of atoms adjacent to the interface[35]. Furthermore, some specific Voronoi polyhedrals at different ACI were shown to exist geometrically to facilitate geometrical transition between two distinct phases[15,36].

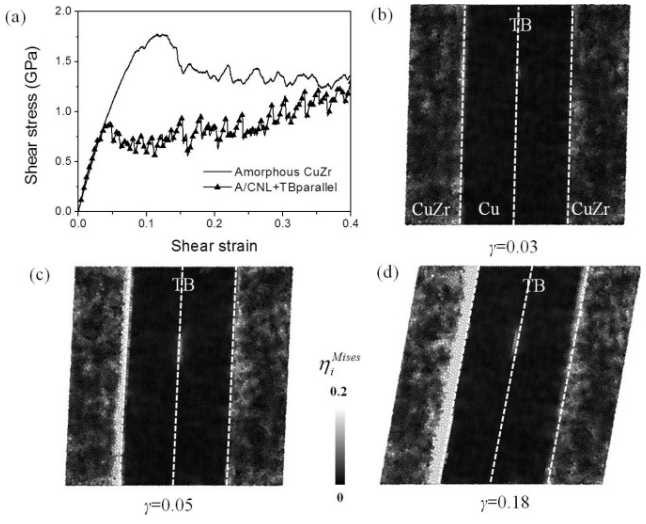

Fig. 4 (a) Stress versus strain curves of A/CNL+$TB_{parallel}$ compared to pure amorphous CuZr. (b) (c) (d) Microstructure evolution snapshots of A/CNL+$TB_{parallel}$ model at engineering shear strain of 0.03, 0.05 and 0.18.

We analyzed next the atomic structures parallel to the A/C interfacial plane of both [110] and $[1\bar{1}\bar{1}]$ interfaces. Atomic plane slices of x = 4.8 nm, 5.0 nm and 5.2 nm were presented in Fig. 5(a). Interfacial orientations relative to the Cu lattice [110] and $[1\bar{1}\bar{1}]$ were analyzed in Figs. 5(b) and (c), respectively. For both interfacial orientations, the radical distribution function (RDF) showed an obvious transition from the long-range disorder to long-range order from the crystalline layer to amorphous layer. On the other hand, the RDF curves at x = 5.0 nm illustrated that the structural transition for $[1\bar{1}\bar{1}]$ interfacial orientation was more abrupt than that for [110]. The atomic structures of the three plane slices at ACIs also showed different degrees of compositional mixing for [110] and $[1\bar{1}\bar{1}]$ crystalline orientations. For [110] interface, more Zr atoms diffusion and lattice distortion could be seen at x = 5.0 nm, and some crystalline lattice arrangement even remained in the amorphous layer at x = 4.8 nm. For $[1\bar{1}\bar{1}]$ interface, however, less compositional mixing was seen at the layer transition zone. Severe lattice mismatch between crystalline and amorphous layers increased the A/C interfacial energy, thus more convenient for interfacial sliding.

Due to the high energetic state and special geometric configuration of $[1\bar{1}\bar{1}]$ interfacial orientation, localized interfacial sliding was very easy to initiate at a low shear stress, which should be avoided in practical application. Previously, micro-sliding bands with highly localized atomic shear strain formed at ACI had been studied and two formation mechanisms were proposed[13]: sliding via the growth of STZs at ACI and sliding due to the spreading of dislocation loop at ACI, which were mainly dominated by the thermodynamic treatments of model construction. That is, interfacial sliding first began heterogeneously at some weaker sites induced by the formation of STZs on the amorphous side and at partial dislocations on the crystalline side near ACI, rather than homogeneously along the layer interface. Large atomic shear strain rapidly assembled at the layer interface, eventually inducing a quite early yielding via shear banding sliding along ACI. Subsequent thickening of SB on an amorphous layer was attributed to internal friction via micro-sliding bands swallowed the STZs inside the amorphous layers.

3.3 Influence of crystal boundaries on the shear banding deformation of nanolaminates

Shear banding in A/CNLs was formed via a combination of STZs activations and dislocation activations affected by crystal boundaries. Three kinds of boundaries were related to dislocation activities: the GB and TB in crystalline Cu interior, and the heterogeneous ACI. The coherent and stable TB with the lowest boundary energy were mechanically strong boundaries, and hence the corresponding critical resolved shear stress must be higher than both the GB and

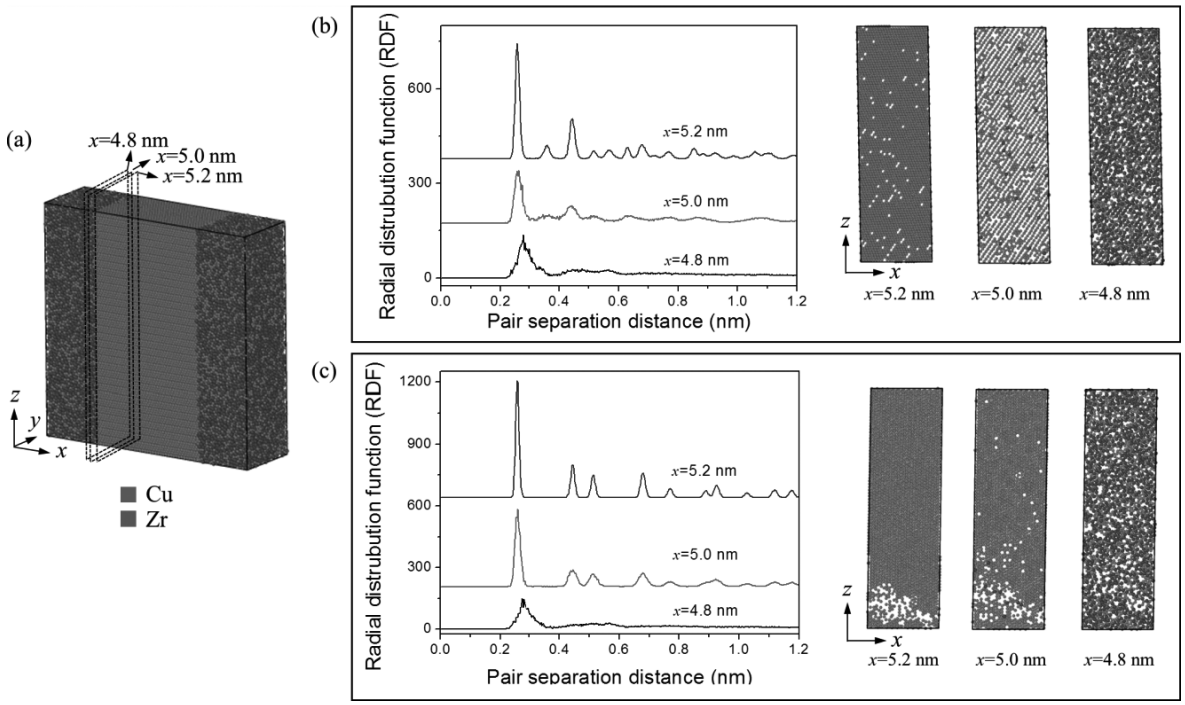

Fig. 5 (a) Atomic structures at ACI, with plane slices of x = 4.8 nm, 5.0 nm and 5.2 nm shown, (b) two-dimensional radial distribution function $g(r)$ of each atomic plane and (c) in-plane atomic structures of [110] and [$1\bar{1}\bar{1}$] interfacial orientations.

ACI. The stress versus strain curves of two A/CNL with GB structures displayed in Fig. 6 showed a moderately high shear strength in comparison with the pure amorphous CuZr and other laminated structures. When the shear strain exceeded about 0.2, the shear stress of A/CNLs+$GB_{parallel}$ was slightly higher than that of A/CNL+$GB_{vertical}$. Another phenomenon was observed from these stress versus strain curves: larger strain bursts appeared in A/CNL+$TB_{parallel}$, A/CNLs+$GB_{vertical}$ and A/CNLs+$GB_{parallel}$ models, while smoother plastic flows occurred in pure amorphous CuZr, A/CNL without boundary and A/CNL+$TB_{vertical}$ models. Note that dislocation activation was an abrupt event, which would lead to series of large strain bursts in stress versus strain curves, while free volume or STZ activation was relatively smooth. For the models considered here, this magnitude discrepancy of strain bursts was mainly because the dominant plastic carriers during shear banding deformation were different.

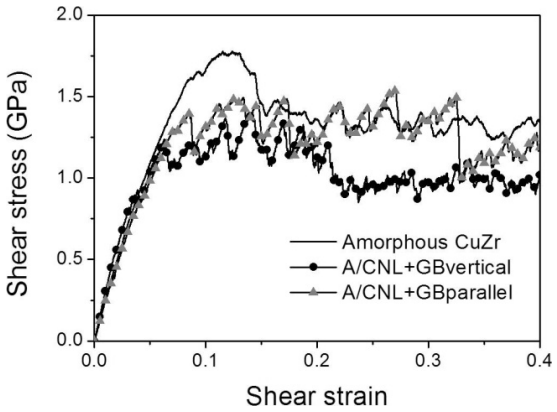

Fig. 6 Stress versus strain curves of A/CNL+$GB_{vertical}$ and A/CNL+$GB_{parallel}$ compared with that of pure amorphous CuZr.

3.3.1 Grain boundary dislocation induced shear banding formation

The plastic deformation snapshots of A/CNL+$GB_{vertical}$ were displayed in Figs. 7(a), (b) and (c), with FCC structure atoms in crystalline Cu layer deleted to clearly show the evolution of lattice defects. Changes in dislocation types and dislocation numbers during plastic deformation were presented in Fig. 7(d). It was seen that Shockley partial dislocations 1/6<112> dominated the whole plastic deformation and, for each type of dislocation, the dislocation number remained constant as the engineering shear strain was increased. Therefore, how these dislocations sustained the plastic deformation by keeping their numbers unchanged needs to be explored next.

For the GB configuration considered here, a large number of defect structures was presented around the GB plane after the initial structure relaxation. At the initial stage of deformation, atomic shear strain accumulated in the vicinity of GB and ACI, due mainly to the high boundary energy and the large number of pre-existing dislocations at the vertical GB of A/CNL+$GB_{vertical}$. Upon loading, the amount of GB ledges would energetically intensify interfacial atomic rearrangement in order to distribute the concentration stress. Based on the geometric condition[37], interfacial dislocations would firstly emit from the triple junction of GB and ACI. Once lattice dislocations were initiated, they could move into grain interior or move along GB. However, because the disordered arrangement and high energetic state of GB would provide a favorable condition for dislocation sliding along GB, nearly all of the dislocation activities and defect structural evolutions were confined within the GB affected zone. A large portion of plastic strain could be accommodated by local structure rearrangement at GB by changing

the magnitude of Burgers vector of pre-existing interfacial dislocations. In such cases, rather than the Schmid factor, the geometric condition of boundary was the determining factor for plastic accommodation. As a result, interfacial atomic rearrangement at GB and dislocation sliding along GB dominated the plastic deformation of the crystalline layer. Meanwhile, atomic strain concentration in the amorphous layer locally accumulated at the junction of GB and ACI neighboring sites, which promoted shear localization in amorphous layers. Finally, the combination of dislocation activations along the GB and shear localization in the amorphous layer caused the formation of a crossover shear banding through the amorphous layer and the crystalline layers.

3.3.2 Dislocation traversing grain boundary delayed shear banding

For A/CNL+GB$_{parallel}$ model, Fig. 8 presented the plastic deformation snapshots and dislocation number variation for each dislocation type during plastic deformation. The number of dislocations showed a rapid increase at the shear strain of 0.1 and remained unchanged afterwards. Before the engineering shear strain exceeded 0.08, local atomic strain primarily accumulated at GB and ACI. As the strain reached 0.09, interfacial dislocation sliding in the right grain of Fig. 8(a) was activated from the ACI. Subsequently, it encountered the paralleled GB which acted as a dislocation wall, thus causing dislocation pile-ups on the way of dislocation motion. As the applied strain was further increased, slip plane in the left grain was activated when the required threshold shear stress was reached.

It should be noticed that, the large number of interfacial dislocation pile-ups caused part of the GB to twist and then transfer across it when the applied strain reached 0.16. It had been established that the interfacial dislocation emission-absorption process and GB twist were closely related. Upon shearing deformation, the energetically instable ACI would stir up a series of interfacial dislocation movements. Significant dislocation emissions and absorptions at GB could result in local destruction and discontinuity of GB structures[38,39]. Once interfacial dislocations encountered the boundaries, they might be piled up or absorbed, giving rise to additional boundary sliding and migration processes[40,41]. As a result, the local GB twist as shown in Fig. 8(b) was caused, which required a higher stress and larger plastic strain in stark contrast with the deformation mechanisms operating in A/CNL+GB$_{vertical}$. With a large number of dislocations blocked at the GB and part of the GB twisted, slip transmission across the GB might happen. Slip transmission across a GB was mainly dependent on three steps, namely, dislocation climb along the boundary, dissociation and recombination of boundary defects, and nucleation of dislocation in adjoining layer. The dislocation climbing force stemmed mainly from the chemical force induced by unbalanced vacancy and the normal stress induced by applied force. When a new dislocation was nucleated at the adjoining side of GB, dislocation slip would transmit across the GB. Kacher *et al.*[42] reported that, as the applied strain was increased, dislocation sliding transmission might induce the activation of additional sliding systems or the emission of perfect dislocations (instead of partial dislocations). Besides, the energy barrier for slip transmission across GB and the

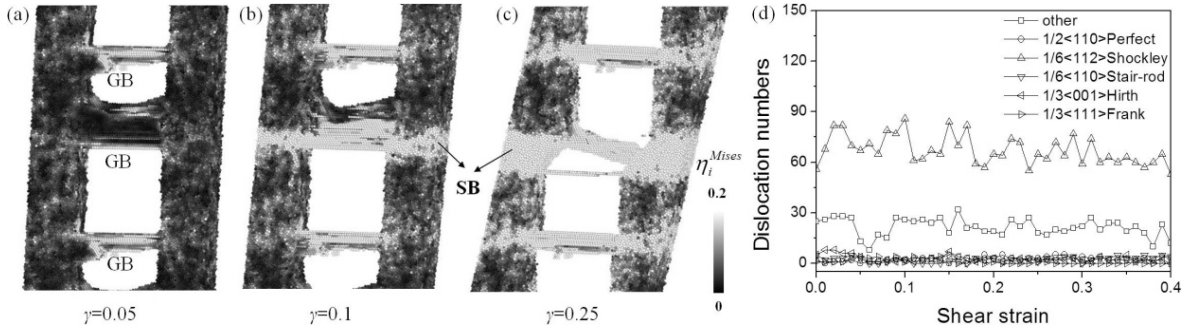

Fig. 7 Shear-banding deformation snapshots of A/CNLs+GB$_{vertical}$ model at engineering strain of (a) 0.05, (b) 0.1 and (c) 0.25, with FCC structure atoms in crystalline Cu layer deleted; (d) variation trends of dislocation type and number during plastic deformation.

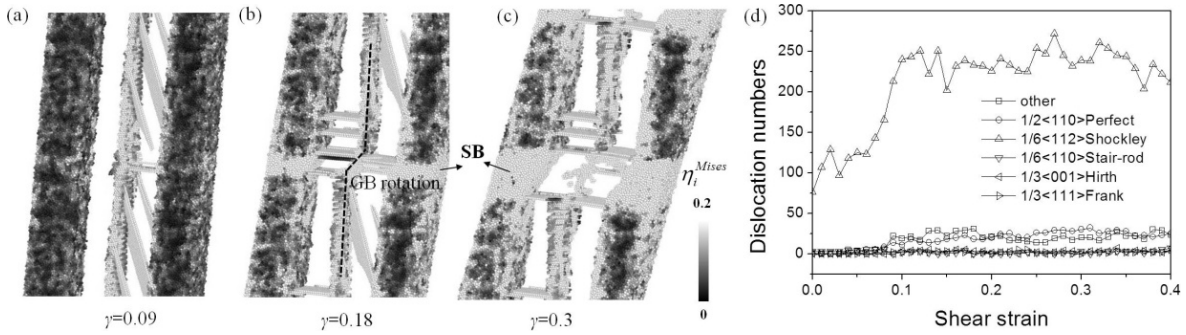

Fig. 8 Shear-banding deformation snapshots of A/CNLs+GB$_{parallel}$ at engineering strain of (a) 0.09, (b) 0.18 and (c) 0.3, respectively, with FCC structure atoms in crystalline Cu layer deleted; (d) variation trends of dislocation type and number during plastic deformation.

energy needed to nucleate a dislocation from GB were found to be inversely proportional to the static GB energy[43]. After a large number of dislocation sliding transmissions, the strain concentration sites in the two neighboring amorphous layers were connected. As a result, a transverse SB formed across both the amorphous layer and the crystalline layer.

Although the plastic deformations of the two A/CNL structures with GB configuration both showed that the SBs propagated across both the amorphous layer and the crystalline layer, the formation of mature SB in A/CNL+$GB_{vertical}$ happened at the engineering shear strain of 0.09 while that in A/CNL+$GB_{parallel}$ model at 0.16, suggesting that A/CNL+$GB_{parallel}$ was an harder configuration for SB deformation. That was mainly because the dislocation slip transmission across the parallel GB and the resulting local GB torsion postponed the shear banding formation.

Despite the results presented above, a large gap remains between the simulation findings and experimental results because, in practice, the microstructures of crystalline layers are more complex than those assumed by the simulation models. For instance, plastic deformation of crystalline layers in A/CNLs was mainly controlled by dislocation nucleation in MD simulations but determined by dislocation propagation in experiments. Further, the uneven grain size distribution and influence of neighboring grains on slip transmission would affect dislocation-boundary interactions in A/CNLs. Although shear banding formation sites were discussed in the present study based on different crystal boundaries in the crystalline layer, many interesting questions are left for further study. For example, the influence of GB or TB inclined to ACI and subsequent dislocation-TB interactions on the strength and ductility of A/CNLs needs further investigation.

4. Conclusions

Interface-related plastic deformation of amorphous $Cu_{55(at\%)}Zr_{45(at\%)}$/crystalline Cu A/CNLs was investigated using MD simulation models. With prevalent microstructural defects in as-deposited crystalline layers of A/CNLs accounted for, the influence of heterogeneous ACI and homogeneous GB and TB in crystalline Cu interior on the shear banding deformation of CuZr/Cu A/CNLs were systemically studied. It was found that interfacial crystal orientation had great influence on the plastic deformation of A/CNLs, and the parallel ACI to dislocation slip plane was much easier to shear and hence should be avoided in practice. The coherent and structural stable TB was prone to induce shear banding localized in the mechanically softer ACI and the amorphous layer interior. The vertical GB in A/CNLs facilitated a transverse shear band across both the amorphous layer and the crystalline layer, assisted by a large number of dislocation activations at GB. Because of the pre-existing lattice defects at the vertical GB, shear banding propagation across both the amorphous and crystalline layers mostly emerged from the GB plane. On the contrary, dislocation slip transmission across the parallel GB and the resulting local GB torsion postponed the shear banding formation.

Acknowledgements

The present work was supported by the National Natural Science Foundation of China (51171141, 51271141, and 51471131) and the Fundamental Research Funds for the Central Universities.

REFERENCES

1) Y.M. Wang, J. Li, A.V. Hamza, *et al.*: Proc. Natl. Acad. Sci. USA **104** (2007) 11155.
2) J.-Y. Kim, D.C. Jang and J.R. Greer: Adv. Funct. Mater. **21** (2011) 4550.
3) J.Y. Zhang, G. Liu, S.Y. Lei, *et al.*: Acta Mater. **60** (2012) 7183.
4) I. Knorr, N.M. Cordero, E.T. Lilleodden, *et al.*: Acta Mater. **61** (2013) 4984.
5) W. Guo, E. Jägle, J. Yao, *et al.*: Acta Mater. **80** (2014) 94.
6) Y. Cui, O.T. Abad, F. Wang, *et al.*: Sci. Rep. **6** (2016) 23306.
7) J.Y. Zhang, G. Liu and J. Sun: Acta Mater. **66** (2014) 22.
8) C. Brandl, T.C. Germann and A. Misra: Acta Mater. **61** (2013) 3600.
9) Y. Wang, J. Zhou, S. Zhang, *et al.*: Mater. Des. **51** (2013) 88.
10) S. Yamamoto, Y.-J. Wang, A. Ishii, *et al.*: Mater. Trans. **54** (2013) 1592.
11) T. Koseki, J. Inoue and S. Nambu: Mater. Trans. **55** (2014) 227.
12) M.C. Liu, J.C. Huang, Y.T. Fong, *et al.*: Acta Mater. **61** (2013) 3304.
13) K.G. Chen, S.Q. Shi, W.J. Zhu, *et al.*: Comput. Mater. Sci. **109** (2015) 266.
14) Y. Cui, Y. Shibutani, S. Li, *et al.*: J. Alloy. Compd. **693** (2017) 285.
15) G.Q. Yang, X.Z. Gao, J.F. Li, *et al.*: J. Appl. Phys. **117** (2015) 015303.
16) W. Guo, E.A. Jagle, P.P. Choi, *et al.*: Phys. Rev. Lett. **113** (2014) 035501.
17) A. Donohue, F. Spaepen, R.G. Hoagland, *et al.*: Appl. Phys. Lett. **91** (2007) 241905.
18) T.G. Nieh and J. Wadsworth: Intermetallics **16** (2008) 1156.
19) C. Rentenberger, T. Waitz and H. Karnthaler: Scr. Mater. **51** (2004) 789.
20) K. Wang, D. Wang and F.S. Han: Lixue Xuebao **32** (2016) 181.
21) S. Sakano and Y. Matsumura: Mater. Trans. **58** (2017) 813.
22) H.Y. Song, Y.L. Li and M.R. An: Comput. Mater. Sci. **84** (2014) 40.
23) P.J. Imrich, C. Kirchlechneriz and G. Dehm: Mater. Sci. Eng. A **642** (2015) 65.
24) N. Li, J. Wang, S. Mao, *et al.*: MRS Bull. **41** (2016) 305.
25) F. Sansoz, K. Lu and T. Zhu: MRS Bull. **41** (2016) 292.
26) H. Kitahara, M. Tsushida and S. Ando: Mater. Trans. **57** (2016) 1246.
27) L. Li, P. Zhang, Z. Zhang, *et al.*: Acta Mater. **73** (2014) 167.
28) S. Plimpton: J. Compu. Phys. **117** (1995) 1.
29) M.I. Mendelev, D.J. Sordelet and M.J. Kramer: J. Appl. Phys. **102** (2007) 043501.
30) A. Hasnaoui, H.V. Swygenhoven and P.M. Derlet: Phys. Rev. B **66** (2002) 184112.
31) M.L. Falk and J.S. Langer: Phys. Rev. E Stat. Phys. Plasmas Fluids Relat. Interdiscip. Topics **57** (1998) 7192.
32) F. Shimizu, S. Ogata and J. Li: Mater. Trans. **48** (2007) 2923.
33) J.P. Palafox-Hernandez, B.B. Laird and M. Asta: Acta Mater. **59** (2011) 3137.
34) Y. Yang, D.L. Olmsted, M. Asta, *et al.*: Acta Mater. **60** (2012) 4960.
35) G.Q. Yang, J.F. Li, Q.W. Shi, *et al.*: Comput. Mater. Sci. **86** (2014) 64.
36) X.Z. Gao, G.Q. Yang, B. Xu, *et al.*: J. Alloy. Compd. **647** (2015) 331.
37) R. Ritchie, P. Novak, R. Yuan, *et al.*: J. Mech. Phys. Solids **58** (2010) 206.
38) I.M. Robertson, T.C. Lee, P. Rozenak, *et al.*: Ultramicroscopy **30** (1989) 70.
39) K.J.H. Al-Fadhalah, C.M. Li, A.J. Beaudoin, *et al.*: Acta Mater. **56** (2008) 5764.
40) Y.J. Wei, A.F. Bower and H.J. Gao: Acta Mater. **56** (2008) 1741.
41) M. Wei, Z. Cao and X. Meng: Acta Metall. Sin. **29** (2016) 199.
42) J. Kacher, B. Eftink, B. Cui, *et al.*: Curr. Opin. Solid St. M. **18** (2014) 227.
43) M.D. Sangid, T. Ezaz, H. Sehitoglu, *et al.*: Acta Mater. **59** (2011) 283.